

Evaporation of active drops: Puncturing drops and particle deposits of ring galaxy patterns

Ghansham Rajendrasingh Chandel , Vishal Sankar Sivasankar, and Siddhartha Das ^{*}
Department of Mechanical Engineering, University of Maryland, College Park, Maryland 20742, USA



(Received 4 August 2023; accepted 8 March 2024; published 27 March 2024)

By virtue of self-propulsion, active particles impart intricate stresses to the background fluids. We propose that this active stress can be utilized to greatly control evaporation dynamics of active drops. We discover a new phenomenon of puncturing of the active drops, where the air-liquid interface of the drop undergoes spontaneous tearing and there occurs a formation of a new three-phase contact line due to the liquid-air interface hitting the liquid-solid interface through evaporation-driven mass loss. Post puncturing, we see an inside-out evaporation of the drop, where the new contact line sweeps towards the pinned outer contact line of the drops, contrasting regular drops that straightaway shrink to zero volume with self-similar shape. Furthermore, we describe how the activity inside the drops can manipulate the three-phase contact-line dynamics, which for contractile drops can result in an up to 50% enhanced lifetime of the drop and 33% quicker evaporation for extensile drops. By analyzing the flux distribution inside the drop, we gain insights on nonintuitive deposition patterns (e.g., ring galaxy type deposits that demonstrate controllable spatial gradients in the concentrations of the deposited particles) of active particles, which are oftentimes biological substances or bimetallic nanoparticles of interest. Finally, we argue that such unique evaporation and particle deposition dynamics can be leveraged for altering the lifetime of drops for bioapplications and for creating customized thin-film deposits with potential three-dimensional printing applications.

DOI: [10.1103/PhysRevFluids.9.033603](https://doi.org/10.1103/PhysRevFluids.9.033603)

I. INTRODUCTION

Active drops are liquid drops consisting of particles that derive energy from their surroundings to produce mechanical work, typically by self-propulsion or induction of active stresses [1–4]. Multiple studies have focused on understanding the fundamentals of active drops [5–14], and found applications in developing active emulsions [15–18] and droplet microswimmers [19–21], enhancing liquid-liquid mixing [22], explaining biolocomotion [23], triggering molecular-scale assembly [24], providing growth models for protocells [25], enforcing control of cargo delivery [26], etc.

While it is fundamental to understand the physics of self-assembly of active particles, the natural progression should be the ability to control the patterning of these particles. Towards this end, researchers have employed vesicles filled with suspension of active particles [27], micropatterning the substrate [28], and chemotaxis [29,30] among other techniques to control the self-assembly of active particles. However, leveraging the fluid flux induced by the evaporation, coupled with active stress, remains an unexplored territory in the context of self-assembly-driven patterning of active particles. Furthermore, recognizing that evaporation serves as a natural endpoint for any unattended fluid drop or film, it becomes crucial to understand the interplay between active stress

*sidd@umd.edu

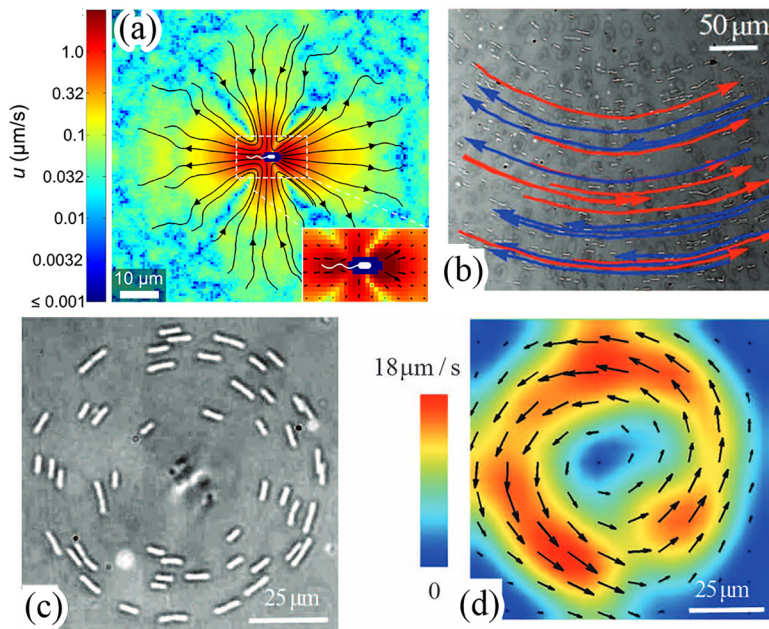


FIG. 1. Experimental relevance for the proposed system. (a) Zero-force swimmer (active particles) producing stress as force dipole (nematic shakers) at far field (reproduced from Drescher *et al.* [37]). (b)–(d) Active swimmers moving in vortex defect (reproduced from Peng *et al.* [31] with permission from AAAS).

and evaporation. In this paper, we describe a hitherto unexplored topic of the evaporation of an active drop [with vortex/pure bend/ $(1, \pi/2)$ defect [31–35]; see Figs. 1(b)–1(d)] and the associated particle deposition pattern formation. The findings of this study apply to drops laden with particles that produce stress in the background fluids described by $\sigma^a = -\xi pp$. Examples of such particles are melanocytes (or nematic shakers) [36] and polar swimmers such as spermatozoa, *Escherichia coli*, biflagellated algae, etc., which generate force dipoles (i.e., shakers) like stress to leading order [37] [see Fig. 1(a)]. For such systems, first, we discover the formation of punctured drops: the active stresses coupled with evaporation-triggered mass loss, force the air-liquid interface of the drop to descend and hit the substrate. The result is the formation of a new contact line (inner contact line, or ICL) and a doughnut-shaped drop. Second, unlike regular drops, active stress constrains the outer contact line (OCL) to remain pinned, while the ICL sweeps at a receding contact angle triggering an inside-out evaporation. Third, such specific drop shape and evaporation dynamics causes particle deposits of a ring galaxylike pattern, characterized by an outer ring and an inner diffuse zone of particles. Such unique punctured drop dynamics and the particle deposition pattern are realized for extensible drops with a certain combination of dimensionless parameters characterizing the activity, aspect ratio, and the receding contact angle. Finally, a comparison with contractile and regular drops demonstrates that activity strongly controls evaporation times and can aid in manipulating contact-line dynamics.

II. MATHEMATICAL FRAMEWORK

We consider the evaporation of a drop laden with active particles. Figure 1 provides the schematic of such a drop as well as the definition of different quantities used to describe the problem. Considering the evaporation to be diffusion dominated [38–41], the equations describing the

evaporation of the active drop can be expressed as (modifying the equations for nonevaporating active drops [3])

$$\partial_t h + \nabla_{\perp} \cdot (\Delta h \bar{\mathbf{u}}_{\perp}) + J_z / \rho = 0, \quad (1a)$$

$$\bar{\mathbf{u}}_{\perp} = \frac{(\Delta h)^2}{3\mu} [\nabla_{\perp} \gamma \nabla_{\perp}^2 h - (\nabla \cdot \boldsymbol{\sigma}^a)_{\perp}], \quad (1b)$$

$$\nabla^2 c = 0, \quad (2a)$$

$$\mathbf{J} = D \nabla c. \quad (2b)$$

Here, h is the local drop height, Δh is the film thickness ($\Delta h = h$ when the substrate is at $z = 0$; see Fig. 1), $\bar{\mathbf{u}}_{\perp}$ is the average in-plane velocity, and ∇_{\perp} represents gradient in the normal plane. γ , μ , and ρ are the surface tension, dynamic viscosity, and drop density. Furthermore, J_z is the evaporation flux in z direction and $\boldsymbol{\sigma}^a = -\xi(\mathbf{r}, t) \mathbf{p} \mathbf{p}$ is the nematic stress tensor [3,4,42–44] (\mathbf{p} and ξ are the polarization field and the effective particle concentration). We consider vortex defect, i.e., $\mathbf{p} = \hat{\theta}$, which is one of the stable topological defects of nematic field and satisfies the anchoring boundary condition by default [3,4,45–47]. Lastly, c is the water vapor concentration (see Fig. 1) and D is the diffusivity of vapor in air.

Since we consider slow, natural evaporation, we solve Eqs. (1) and (2) under the assumption that at a given time, $\xi(\mathbf{r}, t)$ remains uniform in space [i.e., $\xi(\mathbf{r}, t) = \xi(t)$]. Such uniformity, as will be explained below, is possible for low Peclet number, i.e., $\text{Pe} = u_0 R / D_{\xi} \ll 1$, where D_{ξ} is the diffusivity of active particles, u_0 is the characteristic velocity (we consider volume-averaged radial velocity for our problem), and R is the radius of the drop. Let us now look into the situation where this assumption of $\text{Pe} \ll 1$ will hold. $\text{Pe} \ll 1$ implies that the flow of the background fluid is arbitrarily slow, while the diffusion of the particles and particle-particle interactions becomes dominant. For typical evaporation of a 1-mm water drop ($R \sim 1$ mm) under ambient conditions, one obtains $u_0 \sim 10^{-7}$ m/s, except in the vicinity of the three-phase contact line at the very late stages of evaporation [38]. Also, one can consider $D_{\xi} \sim 10^{-9}$ m²/s, which is the typical diffusivity of active particles like bacteria [48]. Under such conditions, $\text{Pe} = u_0 R / D_{\xi} \sim 0.1 \ll 1$. Under such circumstances of $\text{Pe} \ll 1$, there occurs an even distribution of particles inside the drop, i.e., one can ensure a constant density of active particles inside the drop. At increasing velocities, on the other hand, the flow inside the drop will drive the particles towards the edges of the drop, while the diffusive flux will “push” the particles against the concentration gradient. Please note that our assumption of spatially constant density strengthens with increasing humidity and decreasing ambient temperature. Under such circumstances, if the drop is not saturated with particles, the total particles in the drop stays constant, i.e.,

$$\int_{V(t)} \xi(\vec{\mathbf{r}}, t) dV = \xi_0 V_0 \Rightarrow \xi(t) = \frac{\xi_0 V_0}{V(t)}, \quad (3)$$

where ξ_0 represents the initial concentration of the particles inside the drop (of initial volume V_0). Typical to studies on drop evaporation, in Eq. (1b), the magnitude of $\bar{\mathbf{u}}_{\perp}$ is assumed to be much smaller than the speed at which the drop relaxes when perturbed. In other words, at timescales of evaporation, the drop appears to be quasistatic (i.e., in stress equilibrium at all times). This stems from the fact that the change in the shape of the drop is triggered by the volume loss due to the drop evaporation. If the drop attains the new stress-equilibrium state corresponding to the new volume and the new particle concentration much faster than the rate at which the volume changes, *we will observe the drop in a stress-equilibrium state at all times*. From Eqs. (1a) and (1b), we compare the characteristic time τ_{evap} (associated with the change in drop height due to evaporation) with the characteristic times $\tau_{\text{surface tension}}$ (dictating the stresses due to the surface tension effect) and $\tau_{\text{active stress}}$ (timescale associated with the active stresses). For reference, we assume a drop of water showing activity at ambient conditions and find that $\tau_{\text{evap}} > \tau_{\text{surface tension}} \times 10^4$ and $\tau_{\text{evap}} > \tau_{\text{active stress}} \times 10^3$ – 10^5 (see Appendix D for detailed calculations). These conditions imply

that the quasistatic drop assumption remains valid. Under such circumstances, for axisymmetric drop, Eq. (1b) reduces to (see Appendix A for the detailed derivation)

$$\gamma \frac{\partial}{\partial r} \left[\frac{1}{r} \frac{\partial}{\partial r} \left(r \frac{\partial h}{\partial r} \right) \right] + \frac{\xi(t)}{r} = 0. \quad (4)$$

Equation (4) can be solved analytically (see Appendix A) in the presence of the condition $h[r = R(t), t] = 0$ [$R(t)$ is the drop radius; see Fig. 3(k)] yielding

$$h(r, t) = -\frac{\xi(t)}{4\gamma} \left[r^2 \ln \left(\frac{r}{R(t)} \right) + [R(t)^2 - r^2] \right] + \frac{\Theta(t)}{2R(t)} [R(t)^2 - r^2] + C(t) \ln \left(\frac{r}{R(t)} \right). \quad (5)$$

To satisfy Eq. (1a), constants of integration in Eq. (5) [namely, $\Theta(t)$ and $C(t)$] and the unknown drop spreading radius, $R(t)$, must be functions of the evaporation timescale. Using thin-film approximation and assuming initial pinned-contact-line evaporation stage, we can employ the volume conservation condition to evaluate $\Theta(t)$ [38]:

$$\dot{V} = \frac{d}{dt} \int_{r_{\text{in}}}^R h(r, t) 2\pi r dr = - \int_{r_{\text{in}}}^R \frac{J(r) 2\pi r dr}{\rho}. \quad (6)$$

For the pinned CL stage, $r_{\text{in}} = 0$ and $R(t) = R$. For continuity at $h(0, t)$ during the pinned stage, $C(t) = 0$. Using Eqs. (3) and (6), Eq. (5) can be rewritten to provide the dimensionless height, H , as (see Appendix A for the details)

$$H(a, T) = -\frac{\Lambda}{1-T} (a^2 \ln(a) + (1-a^2)) + \left(\frac{\Omega}{2} (1-T) + \frac{3\Lambda}{4} \frac{1}{1-T} \right) (1-a^2). \quad (7)$$

Here $H = h/R$, $T = -t\dot{V}/V_0$, $a = r/R$, $\Omega = 4V_0/\pi R^3$ (aspect ratio), and $\Lambda = \xi_0 R/4\gamma$ (dimensionless activity).

Equation (7) is valid until the time $T < T_p$; for $T > T_p$ ($T_p = 1 - \sqrt{\Lambda/2\Omega}$ is the dimensionless puncturing time), for extensile drops (i.e., $\Lambda > 0$), Eq. (7) yields $H(a=0, T) < 0$, i.e., the air-liquid interface of the drop goes below the substrate and hence the solution no longer holds. We must resolve this issue as the solution must remain physical until the drop evaporates to zero volume.

According to the contact-angle hysteresis (CAH) model proposed by [49,50], contact lines with contact angles θ , such that $\theta_R < \theta < \theta_A$ (θ_R and θ_A are receding and advancing contact angles), remain pinned. Equation (7) shows that at $T = T_p$, the drop surface (air-liquid interface) touches the ground (at $a = 0$) tangentially (this is the drop puncturing event), and hence the contact angle made by the ICL (caused by puncturing) is zero. This is energetically unfavorable under the CAH model and the contact line at the center must follow a receding motion until $\theta(a_p, T_p^+) = \theta_R$ (a_p is the nondimensional puncturing radius of the drop) [see Fig. 3(c)]. Since we assumed slow, diffusion-driven evaporation, the drop will attain its new stress-equilibrium position almost instantaneously after the puncturing, and we represent this time (nondimensionally) as T_p^+ . This gives us our complete set of boundary conditions, $\theta[a_{\text{in}}(T), T_p^+] = \theta_R$ [a_{in} is the dimensionless inner radius; see Fig. 2(e)], $H[a_{\text{in}}(T), T] = 0$, and $H(1, T) = 0$: these conditions can be used to solve Eq. (1b) [a third-order ordinary differential equation (ODE)] to obtain the drop dynamics *post puncturing*. We see that if $\theta[a_{\text{in}}(T), T] = \theta_R$, where $T > T_p^+$, for any volume or activity, then it is always true that $\theta(1, T) > \theta_R$, which implies that the OCL must remain pinned for a quasistatic extensile drop.

We must employ a numerical solution (see Appendix B) for the drop profile after puncturing ($T > T_p$) as we cannot find an analytical solution to Eq. (2) for a punctured geometry. Therefore, we find $\Theta(t)$ and $C(t)$ numerically (see Appendix A for details) such that the boundary conditions are satisfied along with Eqs. (2a), (2b), and (6). Lastly, we must consider the conservation of particles, i.e., account for the rate of deposition of active particles at inner and outer contact lines to determine $\xi(t)$: this, of course, necessitates solving the transport equation for the polarization field \mathbf{p} [51], which may depend on the exact geometry of active particles. We assume that the density of the active particles remains constant in the late stage of the evaporation, i.e., $\xi(T \geq T_p) = \xi(T_p)$

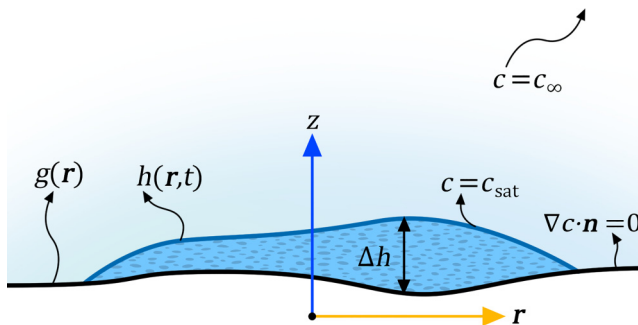


FIG. 2. Schematic of the active evaporating liquid drop having a profile defined by the drop height $h(\mathbf{r}, t)$ (with $\partial_{\perp} h \ll 1$). The drop evaporates on a substrate defined by profile $g(\mathbf{r})$. c denotes the local liquid vapor concentration distribution and \mathbf{n} is the local unit normal vector to the substrate.

post puncturing. In other words, we assume that the reduction in the drop volume is followed by an appropriate deposition of the particles. This is an assumption that is straightforward to let go of, and we can indeed solve the problem even by relaxing this assumption and using a similar analysis for a much more realistic physical solution. The late-stage evaporation (runaway stage) and residual pattern are dictated by the number of particles deposited on the drop edges versus the rise in the concentration of the particles within the drop. The most physical assumption here would be where we set a cutoff or saturation concentration of the particles. Below this saturation concentration, we would see a rise in the particle concentration inside the drop, while above the saturation concentration, the particles would precipitate out of the receding drop.

The reason we made this simplifying assumption of density remaining constant (the drop density being in the saturated zone) during contact-line receding is because introducing saturation concentration for active particles would introduce a new free parameter (and hence a new nondimensional parameter) to our solution, which for the most part, will obscure the main physics of the problem without adding any new insights. To be more specific, all the effects reported in this paper, namely, the puncturing of the drops, increase/decrease in evaporation time, inside-out evaporation of the drop, etc., still occur for any (high or low) value of saturation concentration, and the consideration of the saturation concentration would only act as a correction term. For the clarity of understanding, and since constant density during the runaway stage is an acceptable simplification in the community [52], we introduce this assumption to our study (see Appendix B for the details on the corresponding numerical approach).

It is important to note here that the nondimensional time T (identified above) is the time corresponding to physical time t normalized by the time the drop would have taken to evaporate if the rate of evaporation \dot{V} was constant throughout the evaporation process. Since depinning or puncturing causes a reduction in the surface area available for the evaporative flux to exit through, \dot{V} becomes smaller during these stages. Therefore, typically, we will see that the dimensionless evaporation time is greater than 1. This is further discussed in greater detail in Fig. 4.

III. RESULTS AND DISCUSSIONS

A. Dynamics of puncturing-vs-nonpuncturing extensile drops

Figures 3(a) and 3(b) show the time-dependent evaporation dynamics of an extensile drop corresponding to the combination of Λ , Ω , and θ_R that ensures drop puncturing. Figure 3(a) shows the drop profile for the conditions when the contact line (CL) remains pinned during the evaporation. The very last profile in Fig. 3(a) denotes the profile (at $T = T_p$) that corresponds to the onset of puncturing that forms an ICL [see Fig. 3(e)]. Post puncturing, under CAH, the active stress ensures that θ at the ICL becomes equal to a critical value (θ_R) at $T = T_p^+$ and the corresponding

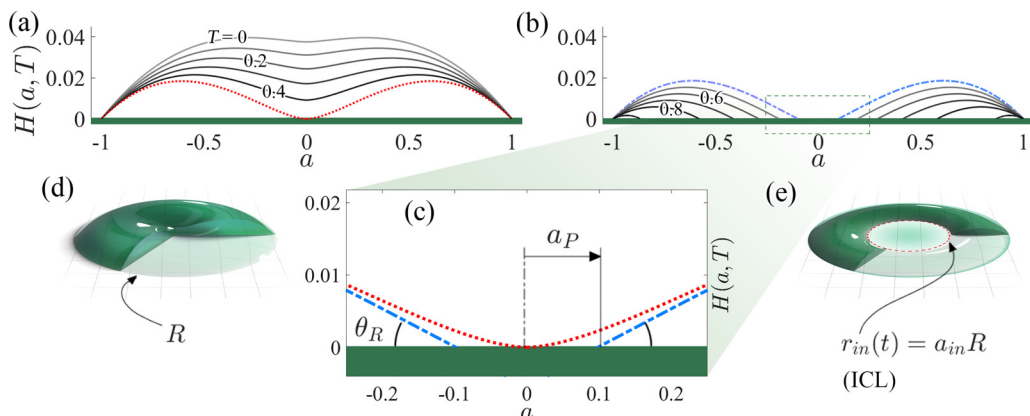


FIG. 3. (a), (b) Height of an evaporating extensile drop undergoing puncturing (for $\Lambda = 0.05$, $\Omega = 0.1$, $\theta_R = 3^\circ$) for (a) time instants (prepuncturing) when the CL is pinned and (b) time instants (postpuncturing) when the puncturing-induced ICL recedes but the OCL remains pinned. (c) Transition from the profile at the onset of puncturing [last profile in 2(a)] to the profile where $\theta = \theta_R = 3^\circ$ and the ICL starts to recede [first profile in 2(b); with dimensionless puncturing radius a_p]. (d), (e) 3D drop profiles corresponding to (d) a prepunctured drop profile ($T = 0.5$) and (e) a postpunctured drop profile ($T = 0.65$). In (e), dimensionless and time-dependent inner radius, $a_{in} = r_{in}/R_0$ is noted. In (a) and (b), the dimensionless times associated with the drop profiles have been identified.

drop profile (from which the ICL starts to recede at evaporation timescales) is the first profile in Fig. 3(b). Figure 3(c) shows this instantaneous transition. Post puncturing, therefore, the motion of the drop [of “doughnut” shape; see Fig. 3(e)], occurs with the ICL receding towards the pinned OCL. Figure 3(b) shows the time evolution of these drop profiles post puncturing. Figures 3(d) and 3(e) respectively provide the three-dimensional (3D) profiles corresponding to the separate drop profiles at prepuncturing (pinned CL) and postpuncturing (receding ICL but pinned OCL) stages. Figures 4(a) and 4(b) provide the evaporating drop profiles for Λ , Ω , and θ_R corresponding to no puncturing for the extensile drop. Figure 4(a) shows the profile for the drop undergoing evaporation with pinned CL. This leads to a progressive decrease in the contact angle eventually leading to the contact angle being equal to θ_R enforcing a subsequent evaporation with the CL receding towards

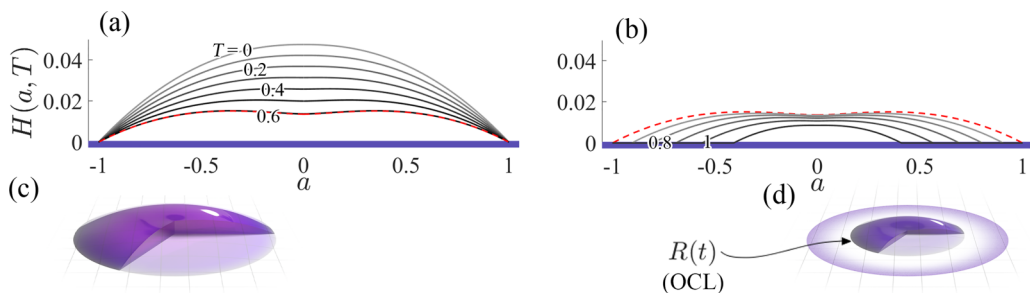


FIG. 4. (a), (b) Time evolution of the profiles of an evaporating extensile nematic drop undergoing no puncturing (for $\Lambda = 0.01$, $\Omega = 0.1$, $\theta_R = 3^\circ$) for (a) time instants when the contact line is pinned and (b) time instants when the contact line recedes. In (a) and (b), the drop profile demarcating the transition between pinned and receding contact-line cases is shown by a dashed line. (c), (d) 3D drop corresponding to the no-puncturing case for (c) $T = 0.603$ (pinned CL case) and for (d) $T = 1$ (receding CL). In (a) and (b), the dimensionless times associated with the drop profiles have been identified.

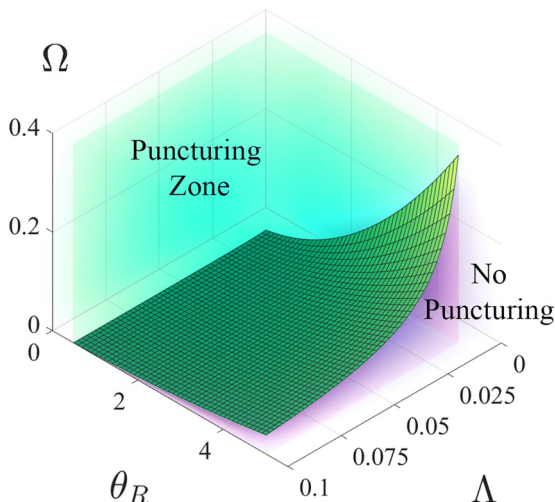


FIG. 5. Parameter space (for parameters Λ , Ω , and θ_R) for determining whether the drop will undergo puncturing or not.

the drop center [shown in Fig. 4(b)]. In the absence of puncturing, the ICL does not form; hence the receding CL motion ensures a progressive shrinkage of the drop [see the corresponding 3D images in Figs. 4(c) and 4(d)]. Finally, in Fig. 5, we provide the parameter space that determines whether the evaporating active drop will undergo puncturing: larger Λ and Ω and smaller θ_R seem to promote drop puncturing.

B. Formation of ring galaxylike deposits

Puncturing of the drop leads to the formation of two separate CLs. As a result, there will be evaporation-driven liquid fluxes in two separate directions (towards each CL). Figure 6(a) provides the direction and magnitude of these fluxes at a time after puncturing for the case studied in Figs. 3(a)–3(e). The fluxes at the ICL and the OCL approach $-\infty$ and $+\infty$, respectively, for $T > T_p$, suggesting particles just adjacent to the CLs are strongly pulled towards the CL by the evaporation-driven mass loss (see [41] for flux distributions for other parameters). Figure 6(b) shows the evaporative flux, J_z , which induces the liquid fluxes: maximum evaporative fluxes occur at the locations of the ICL and the OCL with the ICL progressively receding towards the OCL, which corresponds to increasing $a_{in}(T)$ [Fig. 3(e) defines $a_{in}(T)$]. Correspondingly, the active particles self-assemble and deposit as a single “ring” at the OCL, but they spread out as a diffuse and continuous band (via self-assembly) with progressively decreasing concentration in the direction of motion of the ICL. The eventual result, therefore, is a ring galaxylike deposit [Fig. 6(c)]. The relative concentration of the deposited particles constituting the ring and the diffuse zone depends on (i) the time of the drop puncturing (since the quicker the puncturing, the greater will be the time span for which the ICL exists and recedes, thereby leading to a larger concentration of the particles in the diffuse zone); (ii) the radius of the ICL immediately after puncturing; and (iii) the speed at which the inner contact line recedes (the lesser this speed the greater will be the time that the particles have to get deposited). Figure 6(d) provides the numerical results for the trajectory of the ICL [variation of a_{in} vs T] as functions of Λ and Ω . From this figure, one can also obtain the ICL receding velocity (by estimating the slope). The variation of a_p and the corresponding drop puncturing time (T_p ; see inset), as functions of Λ and Ω , are separately plotted in Fig. 6(e). Finally, Fig. 6(f) provides the schematic of the expected ring galaxy deposition pattern for different combinations of Λ and Ω .

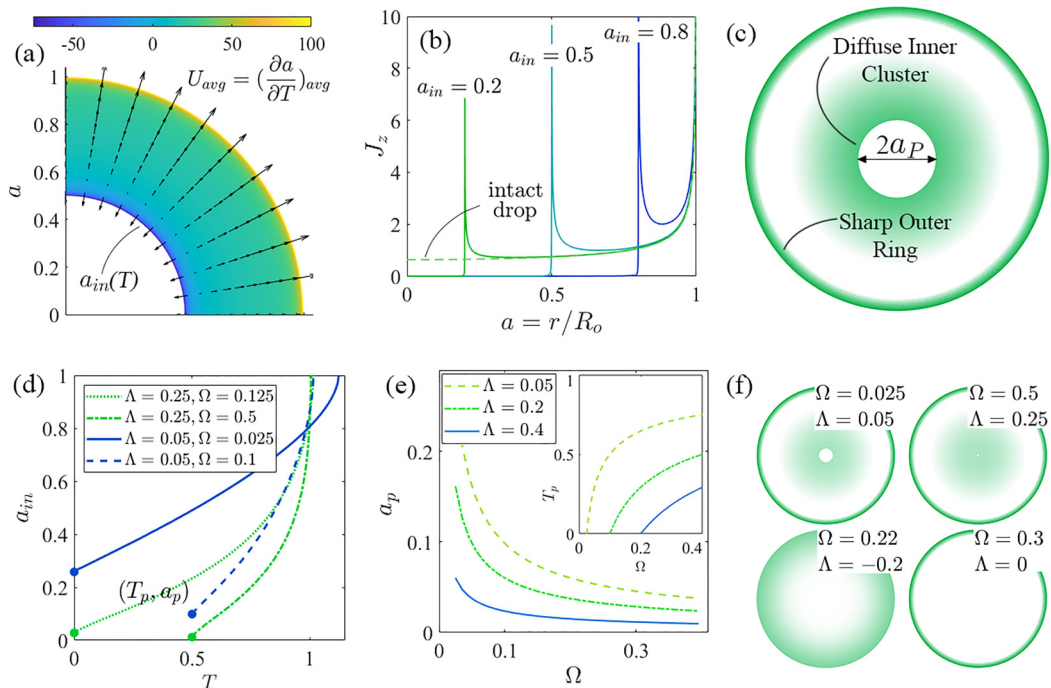


FIG. 6. (a) Top view of the punctured drop showing the liquid fluxes [quantified in terms of the dimensionless velocity field $U_{\text{avg}} = (\frac{\partial a}{\partial T})_{\text{avg}}$] directed towards the ICL and the OCL. Results are shown for $\Lambda = 0.25$, $\Omega = 0.50$, $\theta_R = 3^\circ$, and $T = 0.95$. (b) Flux of vaporized liquid corresponding to different locations of the receding ICL (which correspond to different values of a_{in}) and fixed OCL. (c) Schematic of the ring galaxylike particle deposit pattern. (d) Variation of a_{in} vs T for different Λ and Ω . Nondimensional puncturing time (T_p) and puncturing radius (a_p) [$a_p = (a_{\text{in}})_{T=T_p}$] has been indicated for one of the curves. (e) Variation of a_p and T_p (see inset) with Λ and Ω . (f) Anticipated ring galaxy deposition patterns for different combinations of Λ and Ω .

C. Extensile-versus-contractile drops

In Figs. 3–6, we have considered the dynamics of an extensile drop and the expected particle deposition pattern resulting from the evaporation of such drops. Figure 7(a) provides the time evolution of the drop profiles for the contractile drop characterized by negative activity, i.e., $\Lambda < 0$. There is no puncturing of the drops and the evaporation-driven drop dynamics first occurs with the CL pinned, followed by the receding CL. Contractile drops undergo much slower evaporation (evaporation time can be up to 50% more) as compared to extensile drops. Figure 7(b) shows the dimensionless evaporation time, T_{evap} (time needed for the drop volume to reach zero) as functions of Λ and Ω . For extensile drops that puncture, the evaporation time is significantly small, i.e., much smaller than the nonactive drops ($\Lambda = 0$) with the same aspect ratio. On the other hand, for contractile drops ($\Lambda < 0$), T_{evap} is significantly higher with T_{evap} increasing with $-\Lambda$. The contractile drop contracts and pulls the liquid away from the three-phase contact line and towards the drop center. This reduces the contact angle forcing the contact angle to reach θ_R much earlier, thereby enforcing a quicker onset of the drop dynamics with receding CL. Consequently, the drop wetted radius, R , starts to reduce much earlier for the contractile drops and hence evaporation for contractile drops predominantly occurs at smaller R values. A corollary to this, the depinning is delayed by positive, or extensile activity. Evaporation at a smaller R (for the case of the contractile drop) will lead to a smaller rate of evaporation [as suggested by Eq. (6)], enforcing a greater evaporation time for contractile drops as compared to the extensile and nonactive drops.

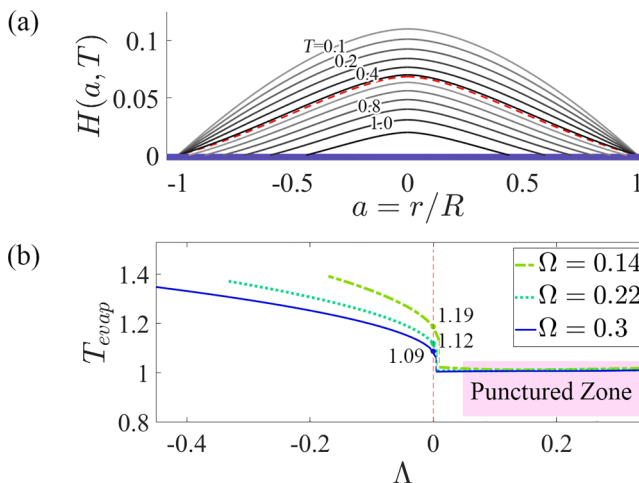


FIG. 7. (a) Time evolution of the profiles of an evaporating contractile drop ($\Lambda = -0.04$, $\Omega = 0.2$, $\theta_R = 3^\circ$). At $T = 0.53$, the contact angle becomes equal to θ_R (profile shown by dashed line). For $T < 0.53$, the drop dynamics occur with pinned CL, while for $T > 0.53$, the drop dynamics occur with receding CL. (b) Variation of the dimensionless evaporation time, T_{evap} , for different values of Λ and Ω . Cases with $\Lambda \leq 0$ correspond to contractile drops. T_{evap} for extensile drops that undergo puncturing and nonactive drops ($\Lambda = 0$) have been separately indicated. In (a), the dimensionless times associated with the drop profiles have been identified.

IV. CONCLUSIONS

In summary, we reveal that the dynamics of active drops under vortex defects is characterized by the formation of punctured drops, ring galaxylike deposits of the nematic particles, and a wide variation in the drop evaporation lifetime. More generally, this study points to the residual structure formed by biological cell organelles/bacteria that show herd behavior and induce active stress. Previously, active stresses have been known to trigger small drop motion; here, we show the use of such active stresses to regulate drop evaporation and evaporation-driven particle patterning. This is the most significant finding of this paper, which also points to possibilities of achieving the desired deposition pattern by engineering the polarization field. The unique ability to control the drop lifetime by changing the nature of the activity (extensile versus contractile) can be leveraged for applications ranging from slow evaporation-driven crystal growth [53] to fast evaporation-driven rapid cooling [54,55] and faster stimulation of bacterial osmoregulation for cell viability assessment [56]. On the other hand, the ability to ensure a ring galaxylike deposition pattern will enable self-assembly-driven fabrication of components (e.g., superhydrophobic surfaces [57], 3D nanostructures [58], photonic crystals [59], etc.) that can have a controllable spatial gradient in the concentration of the constituent materials.

APPENDIX A: ANALYTICAL SOLUTION FOR THE EVAPORATION DROP DYNAMICS PRIOR TO PUNCTURING

The evaporation-driven evolution of the drop height (h) can be expressed by coupling the kinematic boundary condition and the continuity, as expressed below:

$$\partial_t h = (u_z)_{z=h} - (\mathbf{u}_\perp)_{z=h} \cdot \nabla_\perp h - J_z / \rho \quad (\text{kinematic boundary condition}), \quad (\text{A1})$$

$$\nabla_\perp \cdot \mathbf{u}_\perp + \partial_z u_z = 0 \quad (\text{continuity}). \quad (\text{A2})$$

Here, \mathbf{u}_\perp is the in-plane velocity vector field, ∇_\perp represents the gradient in the normal plane, J_z is the evaporation flux in z direction, and ρ is the density of the drop. Integrating Eq. (A2) with

respect to z between the limit $z = g$ to $z = h$ (see Fig. 2), and using Eq. (A1), we can write

$$\partial_t h + \nabla_{\perp} \cdot \int_g^h \mathbf{u}_{\perp} dz + J_z/\rho = 0 \Rightarrow \partial_t h + \nabla_{\perp} \cdot (\Delta h \bar{\mathbf{u}}_{\perp}) + J_z/\rho = 0. \quad (\text{A3})$$

In Eq. (A3), $\bar{\mathbf{u}}_{\perp}$ is the average in-plane velocity vector that can be expressed as

$$\bar{\mathbf{u}}_{\perp} = \frac{\int_g^h \mathbf{u}_{\perp} dz}{h(\mathbf{r}, t) - g(\mathbf{r})} = \frac{\int_g^h \mathbf{u}_{\perp} dz}{\Delta h}. \quad (\text{A4})$$

Please note that Eq. (A3) is Eq. (1a) in this paper.

We now go to the governing equations for the fluid flow inside the drop. Using the Stokes equation under lubrication approximation, we can write

$$\mu \nabla^2 \mathbf{u} - \nabla P - \nabla \cdot \boldsymbol{\sigma} = 0, \Rightarrow \mu \partial_z^2 \begin{bmatrix} \mathbf{u}_{\perp} \\ 0 \end{bmatrix} - \nabla P + \nabla \cdot \boldsymbol{\sigma}^a = 0. \quad (\text{A5})$$

In Eq. (A5), P is the pressure, μ is the dynamic viscosity of the liquid, and $\boldsymbol{\sigma}^a$ is the active stress tensor.

The in-plane ($\hat{\mathbf{r}}$) component of Eq. (A5) can be expressed as

$$\mu \partial_z^2 \mathbf{u}_{\perp} - \nabla_{\perp} P + (\nabla \cdot \boldsymbol{\sigma}^a)_{\perp} = 0. \quad (\text{A6})$$

We assume a parabolic profile for \mathbf{u}_{\perp} in the z direction [3], i.e.,

$$\mathbf{u}_{\perp} = \alpha(r, t) \frac{z(2\Delta h - z)}{(\Delta h)^2} \hat{\mathbf{r}}, \quad (\text{A7})$$

where $\alpha(r, t)$ is an unknown constant.

Using Eq. (A7) in Eq. (A6), we can obtain

$$\alpha(r, t) = \frac{(\Delta h)^2}{2\mu} [\nabla_{\perp} P - (\nabla \cdot \boldsymbol{\sigma}^a)_{\perp}]. \quad (\text{A8})$$

The complete velocity vector field, therefore, can be obtained from Eqs. (A7) and (A8). This velocity vector field, \mathbf{u}_{\perp} , can next be used to obtain the average in-plane velocity vector $\bar{\mathbf{u}}_{\perp}$, i.e.,

$$\bar{\mathbf{u}}_{\perp} = \frac{\int_g^h \mathbf{u}_{\perp} dz}{h(\mathbf{r}, t) - g(\mathbf{r})} = \frac{\int_g^h \mathbf{u}_{\perp} dz}{\Delta h} = \frac{2}{3} \alpha(r, t). \quad (\text{A9})$$

Using Eq. (A9) to replace $\alpha(r, t)$ in terms of $\bar{\mathbf{u}}_{\perp}$, one can write

$$\bar{\mathbf{u}}_{\perp} = \frac{(\Delta h)^2}{3\mu} [\nabla_{\perp} P - (\nabla \cdot \boldsymbol{\sigma}^a)_{\perp}]. \quad (\text{A10})$$

Under lubrication approximation, the pressure inside the drop is impinged from the surface, and its variation along the height of the drop (i.e., the z direction) is negligible. The impinged pressure is given by the Laplace pressure due to surface tension in the fluid “ γ ”, i.e., $P \approx \gamma \nabla_{\perp}^2 h$. Hence, Eq. (A10) reduces to

$$\bar{\mathbf{u}}_{\perp} = \frac{(\Delta h)^2}{3\mu} [\nabla_{\perp} \gamma \nabla_{\perp}^2 h - (\nabla \cdot \boldsymbol{\sigma}^a)_{\perp}]. \quad (\text{A11})$$

Please note that Eq. (A11) is Eq. (1b) in this paper.

We now assume the case where the particles are aligned circumferentially, i.e., $\mathbf{p} = \hat{\boldsymbol{\theta}}$. This leads to

$$\boldsymbol{\sigma}^a = -\xi(\mathbf{r}, z, t) \mathbf{p} \mathbf{p} \Rightarrow (\nabla \cdot \boldsymbol{\sigma}^a)_{\perp} = \frac{-\xi(\mathbf{r}, z, t)}{r} \hat{\mathbf{r}}. \quad (\text{A12})$$

We assume $\xi(\vec{r}, t)$, which is the effective concentration of the nematic particles inside the drop, to be uniform in space at all times; however, we track its value at any given time. The simplest, yet effective model of doing that is by conserving the total amount of particles inside the drop, i.e.,

$$\int_{V(t)} \xi(\mathbf{r}, z, t) dV = \xi_0 V_0 \Rightarrow \xi(t) \int_{V(t)} dV = \xi_0 V_0 \Rightarrow \xi(t) = \frac{\xi_0 V_0}{V(t)}. \quad (\text{A13})$$

This expression for σ^a [obtained by using Eq. (A13) in Eq. (A12)], along with the expression for $\bar{\mathbf{u}}_{\perp}$ [see Eq. (A11)], when substituted in Eq. (A3) gives us our final equation of motion:

$$\partial_t h + \frac{1}{3\mu} \nabla_{\perp} \cdot \left\{ (\Delta h)^3 \left[\nabla_{\perp} \gamma \nabla_{\perp}^2 h - \frac{-\xi(t)}{r} \hat{\mathbf{r}} \right] \right\} + J_z / \rho = 0. \quad (\text{A14})$$

The magnitude of $\bar{\mathbf{u}}_{\perp}$ is assumed to be much smaller than the speed at which the drop relaxes when perturbed. In other words, at timescales of evaporation, the drop appears quasistatic (i.e., in stress equilibrium at all times). Under such circumstances [and using Eq. (A11) to express $\bar{\mathbf{u}}_{\perp}$] one can write

$$\nabla_{\perp} \gamma \nabla_{\perp}^2 h + \frac{\xi(t)}{r} \hat{\mathbf{r}} = 0. \quad (\text{A15})$$

Equation (A15) is Eq. (3) in this paper.

The angular component of Eq. (A15) is identically satisfied by putting $h(r, \theta) = h(r)$. On the other hand, considering the radial component of Eq. (A15), one can write

$$\gamma \frac{\partial}{\partial r} \left(\frac{1}{r} \frac{\partial}{\partial r} \left(r \frac{\partial h}{\partial r} \right) \right) + \frac{\xi(t)}{r} = 0. \quad (\text{A16})$$

Please note that Eq. (A16) is Eq. (4) in the main paper.

The drop height can be obtained by integrating Eq. (A16) thrice with respect to r in the presence of the boundary condition, $h(R, t) = 0$, yielding

$$h(r, t) = -\frac{\xi(t)}{4\gamma} \left[r^2 \ln \left(\frac{r}{R(t)} \right) + [R(t)^2 - r^2] \right] + \frac{\Theta(t)}{2R(t)} [R(t)^2 - r^2] + C(t) \ln \left(\frac{r}{R(t)} \right), \quad (\text{A17})$$

where $\Theta(t)$ and $C(t)$ are (to be determined) constants of integration and $R(t)$ is the unknown drop-spreading radius.

Please note that Eq. (A17) is Eq. (5) in the main paper.

For the pinned CL evaporation stage, $R(t) = R$ is a constant. Also, the condition that $h(0, t)$ is finite during the pinned CL evaporation stage enforces $C(t) = 0$.

We, therefore, now only need $\Theta(t)$ to fully obtain the height profile.

To calculate the evolution of $\Theta(t)$, we need an additional equation, which we get from the rate of evaporation and conservation of the drop volume. Following Marín *et al.* [38], we can write

$$\frac{dV(t)}{dt} = \dot{V} = -\frac{1}{\rho} \int_0^R J(r) 2\pi r dr = -\frac{4RDc}{\rho}. \quad (\text{A18})$$

In Eq. (A18), \dot{V} is the rate of change of drop volume due to evaporation-driven mass loss, D is the diffusivity of the vapor in air, and c is the vapor concentration at the drop surface.

Using Eq. (A18), one can write (with V_0 being the initial volume of the drop)

$$V(t) = V_0 + \dot{V}t. \quad (\text{A19})$$

Also,

$$V(t) = \int_0^R h(r, t) 2\pi r dr \Rightarrow \frac{dV(t)}{dt} = \frac{d}{dt} \int_0^R h(r, t) 2\pi r dr. \quad (\text{A20})$$

Using Eq. (A17) to express $h(r, t)$ and using Eq. (A13) to replace $\xi(t)$, one can use Eq. (A20) to obtain the constant $\Theta(t)$ in terms of \dot{V} [note \dot{V} is expressed using Eq. (A18)] as

$$\begin{aligned} \dot{V}(t) &= -\frac{\xi_0 V_0 \pi}{32\gamma V(t)^2} \dot{V} R^4 + \frac{\xi_0 V_0 \pi}{8\gamma V(t)^2} \dot{V} R^4 + \frac{d\Theta}{dt} \frac{\pi R^3}{4} \Rightarrow \frac{d\Theta}{dt}(t) = \dot{V} \frac{4}{\pi R^3} \left(1 - \frac{3\xi_0 V_0 \pi}{32\gamma V(t)^2} R^4\right) \\ \Rightarrow \Theta(t) &= \Theta(0) + \dot{V} \frac{4}{\pi R^3} \left(t - \frac{3\xi_0 \pi R^4}{32\gamma} \left(\frac{t}{V_0 + \dot{V}t}\right)\right). \end{aligned} \quad (\text{A21})$$

Equations (A21) and (A18) ensure that we have a closed-form expression of the drop height using Eq. (A17). Finally, by trivial algebra, one can reduce the drop height expression to dimensionless form as

$$H(a, T) = -\frac{\Lambda}{1-T} (a^2 \ln(a) + (1-a^2)) + \left(\frac{\Omega}{2}(1-T) + \frac{3\Lambda}{4} \frac{T}{1-T}\right) (1-a^2), \quad (\text{A22})$$

where these different dimensionless quantities can be expressed as

$$H = \frac{h}{R}, \quad T = -t \frac{\dot{V}}{V_0}, \quad a = \frac{r}{R}, \quad \Theta(t) = \Omega(1-T) + \frac{3\Lambda}{2} \left(\frac{1}{1-T}\right), \quad \Omega = \frac{4V_0}{\pi R^3}, \quad \Lambda = \frac{\xi_0 R}{4\gamma}. \quad (\text{A23})$$

Please note that Eq. (A22) is Eq. (7) in the main paper.

APPENDIX B: NUMERICAL (SEMIANALYTICAL) SOLUTION FOR THE POSTPUNCTURING STAGE

One can easily solve the problem of the evaporating drop with the active stresses entirely numerically by adding the active stress as the body force in the Navier-Stokes equation and by utilizing the contact angles hysteresis model in the employed numerical package. Nevertheless, for the present case, it suffices to obtain just the rate of change of volume as a function of inner radius numerically (by employing Computational Fluid Dynamics just one time).

We solve the dynamics of the punctured drop in two steps. First, we get the drop shape (and hence the inner punctured radius, r_{in}) as a function of the drop volume V , the active particle concentration ξ , and the receding contact angle θ_R . This can be done independently of any rate of change of volume. Hence, from the first step, we shall get $r_{\text{in}}(V)$.

In the second step, again independently, we can numerically solve (using COMSOL) the rate of change of drop volume, \dot{V} , as a function of r_{in} . Hence, from the second step, we can get $\dot{V}(r_{\text{in}})$. This will mean that by combining the outputs of steps 1 and 2, we can get $\dot{V}[V(t)]$.

With this, we have an easy-to-solve ODE:

$$\frac{dV(t)}{dt} = \dot{V}[V(t)], \quad (\text{B1})$$

$$\int_{V_0}^{V(t)} \frac{dV}{\dot{V}[V(t)]} = t(V). \quad (\text{B2})$$

As already pointed out, the first step aims to obtain $r_{\text{in}} = r_{\text{in}}(V, \xi, \theta_R)$. For this we need to fix $\Theta(t)$, $R(t)$, and $C(t)$ in Eq. (A17), such that the overall drop volume is V and the contact angle at the ICL is $\theta[r_{\text{in}}(t), t] = \theta_R$. We see that if $\theta[r_{\text{in}}(t), t] = \theta_R$ for any volume or activity, then it is always true that $\theta[R(t), t] > \theta_R$, which implies that the OCL must remain pinned, and hence $R(t) = R$.

Moving further, mathematically, we have three conditions that we must satisfy:

First condition: $h[r_{\text{in}}(t), t] = 0$.

Second condition: The drop volume is V .

Third condition: $\theta[r_{\text{in}}(t), t] = \theta_R$.

We have three free variables, namely, $\Theta(t)$, $r_{\text{in}}(t)$, and $C(t)$, to ensure that these three conditions are satisfied.

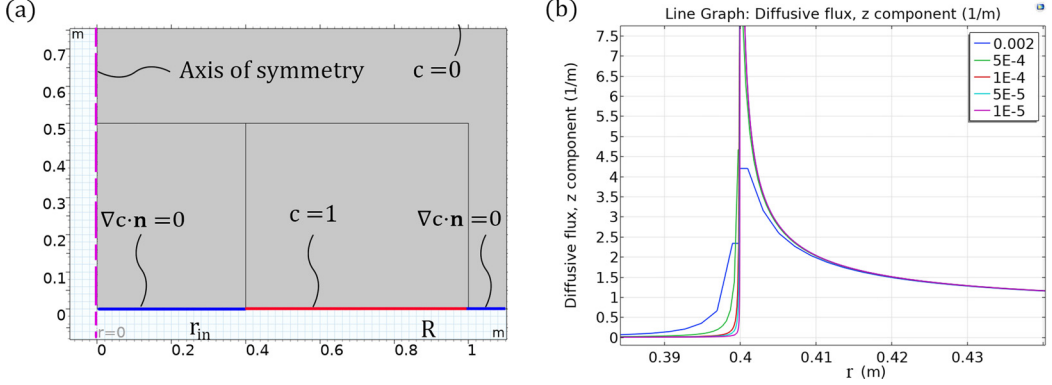


FIG. 8. (a) Zoomed-in snippet of the simulation geometry employed in COMSOL. The bounding box is 50 units \times 50 units, and the drop is a disk of radius $R = 1$ unit with the hole of radius $r_{in} = 0.4$ unit. A boundary condition of $c = 0$ has been imposed on the top and right edges of the box, which are at a distance of 50 units from the center. (b) Zoomed-in plot of $J_z(r)$ vs r for $r_{in} = 0.4$ for different sizes (length units) of the edge elements. We find that negligible difference in the results of the flux variation between the cases with edge elements of sizes 5×10^{-5} units and 1×10^{-5} units.

We can get $\Theta(t) = \Theta(r_{in}, V, C)$ by integrating Eq. (A17), i.e.,

$$V(t) = \int_{r_{in}(t)}^R h(r, t) 2\pi r dr, \quad (\text{B3})$$

and subsequently, isolating $\Theta(t)$, as shown below:

$$\Theta(r_{in}, V, C) = \left(\frac{-4C[-R^2 + r_{in}^2 - 2r_{in}^2 \ln(\frac{r_{in}}{R})] + \frac{8V}{\pi} + \frac{\xi}{4\gamma}[r_{in}^4 - R^4 - 4r_{in}^4 \ln(\frac{r_{in}}{R})]}{(R^2 - r_{in}^2)^2} + \frac{\xi}{\gamma} \right) \frac{R}{2}. \quad (\text{B4})$$

This above form of $\Theta(t)$ guarantees the volume conservation for all $V(t)$, $C(t)$, and $r_{in}(t)$. However, it does not necessarily satisfy $h[r_{in}(t), t] = 0$.

For any given volume $V(t)$, and the constant $C(t)$, there exists a unique $r_{in}(t)$ such that $h[r_{in}(t), t] = 0$. We solve for this $r_{in}(t)$ by fixed-point iteration. In this method, we first guess a radius r_g and find the root of $h(r_g, t) = 0$ for given C and the above-prescribed Θ in Eq. (B4). We update $r_g = r_{g \text{ new}}$. We repeat this process until the desired tolerance is reached, i.e., $h(r_g, t) < 10^{-5}R$. Lastly, we adjust $C(t)$ by linearly varying it until we satisfy our last boundary condition $\theta[r_{in}(t), t] = \theta_R$. Hence, we have a framework to find our drop profile corresponding to any volume $V(t)$ and receding angle θ_R , and the corresponding $r_{in}[V(t)]$. In other words, this first step yields $r_{in}[V(t)]$. Of course, we have to now get this volume $V = V(t)$. The second step, which is a numerical exercise, yields this $V(t)$.

For this second step, to find $V(t)$, we utilize the partial differential equation solving capabilities of COMSOL to solve

$$\nabla^2 c = 0, \quad \mathbf{J} = D\nabla c. \quad (\text{B5})$$

Equation (B5) will be solved numerically with the boundary conditions suggested in Fig. 1. Please note that Eq. (B5) is the same as Eqs. (2a) and (2b) of this paper. Using the axisymmetric nature of the problem, we set up Eq. (B3) in COMSOL [with these boundary conditions (see Fig. 1)] in cylindrical coordinates [see Fig. 8(a)].

We perform our grid convergence and settle with the maximum edge element size of 1×10^{-5} units; as shown in Fig. 8(b), there is negligible difference in the results of the flux variation between the cases with edge elements of sizes 5×10^{-5} units and 1×10^{-5} units.

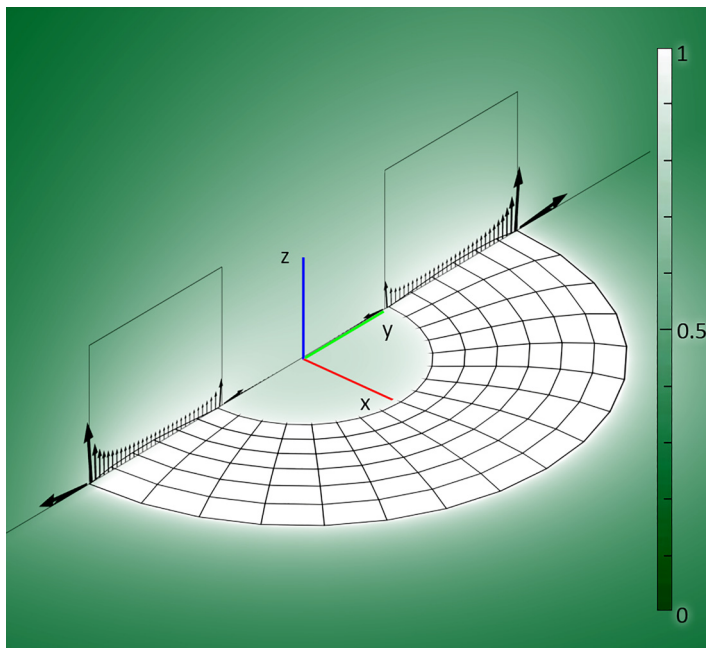


FIG. 9. Numerical simulation result for the flux (shown by arrows) and vapor concentration (shown by color map) distribution across the punctured drop for the time instant when $r_{in} = 0.4$ units and $R = 1$ unit. The dark green represents zero saturation of vapor at a distance far away from the drop, while white represents 100% saturation that is near the drop surface.

Figure 9 provides the flux and vapor concentration distribution at different cross-sectional locations of the punctured drop, obtained from this numerical procedure.

Finally, Fig. 10 provides the numerically obtained rate of change of drop volume as a function of r_{in} , i.e., we get $\dot{V}(r_{in})$. Now from step 1, we have $r_{in}(V)$. Hence, we can combine these two outputs to obtain $\dot{V}(V)$. This $\dot{V}(V)$ can be used in Eq. (B2) to complete the integration and get $V(t)$. Once $V(t)$ has been obtained, we can accordingly obtain $\Theta(t)$, $r_{in}(t)$, and $C(t)$, and hence $h(r, t)$

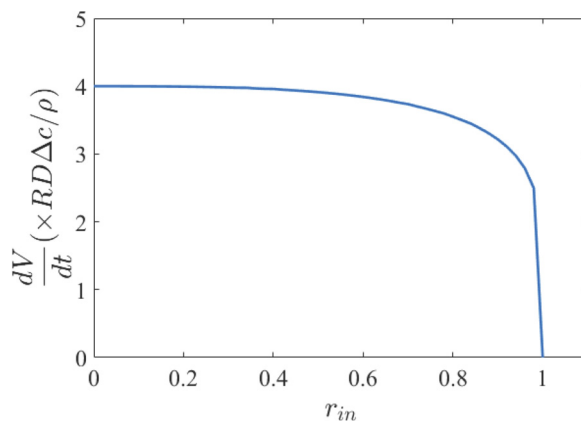


FIG. 10. $\dot{V}(r_{in})$ -vs- r_{in} variation. $\dot{V}(r_{in})$ is in units of $RD\Delta c/\rho$.

(see step 1). We also have $J_z(r)$ for all values of r_{in} , which can be substituted in Eqs. (1b) or (A3) to find flux distribution inside the drop [see Fig. 6(b) of this paper].

This completes our derivation required to get the drop height profiles for any punctured drop.

APPENDIX C: SEMIANALYTICAL SOLUTION FOR THE DEPINNING STAGE (WITHOUT PUNCTURING)

As evident in Figs. 4(c) and 4(d) and Fig. 7(a), extensile drops (for certain combinations of parameters) and contractile drops will not undergo any puncturing; rather they undergo depinning and the subsequent evaporation with receding OCL. Such an occurrence becomes possible since the drop attains the critical receding angle (θ_R) at the OCL before the drop punctures (or the liquid-air interface of the drop hits the substrate), i.e., $T_{dp} < T_p$ (where T_{dp} is the dimensionless time for depinning of the OCL). Obviously, for the case of punctured drops, $T_{dp} > T_p$, and hence there is drop puncturing, formation of the ICL, and the occurrence of evaporation with a receding ICL but a pinned OCL.

These two dimensionless quantities, T_{dp} and T_p , can be expressed as

$$T_{dp} = \frac{2\Omega - \theta_R - \sqrt{-2\Lambda\Omega + \theta_R^2}}{2\Omega}, \quad T_p = 1 - \sqrt{\frac{\Lambda}{2\Omega}}. \quad (\text{C1})$$

Note that this expression for T_{dp} is obtained by employing $(\frac{\partial H}{\partial a})_{a=1} = \theta_R$ in Eq. (A22).

We now solve for the depinning case, where $T_{dp} < T_p$ [i.e., corresponding to the conditions delineated in the purple region indicated in Fig. 1(j) in the main paper for the extensile drops as well as for contractile drops]. At $T = T_{dp}$, the OCL reaches the receding contact angle (θ_R), starts receding, and maintains the receding contact angle at the OCL throughout its lifetime. The form of the drop profile that satisfies this constant contact-angle condition, for any spreading radius $R(t)$, is

$$h(r, t) = -\frac{\xi(T_{dp})}{4\gamma} \left[r^2 \ln \left(\frac{r}{R(t)} \right) + R(t)^2 - r^2 \right] + \left(\frac{\xi(T_{dp})R(t)}{4\gamma} + \theta_R \right) \frac{R(t)^2 - r^2}{2R(t)}. \quad (\text{C2})$$

Here, similar to the situation described in Appendix B, $\xi(T_{dp})$ represents the activity concentration at the time of depinning, which we assume stays constant by appropriate deposition of the particles along its receding contact line. At this stage the volume V is given by

$$V[R(t)] = \int_0^{R(t)} h(r, t) 2\pi r dr = \frac{\pi R(t)^3}{32} \left(8\theta_R - \frac{\xi(T_{dp})}{\gamma} R(t) \right), \quad (\text{C3})$$

which can be inverted to get $R[V(t)]$.

Also, using Eq. (A18), we have the rate of change of volume as a function of the outer radius. Therefore, we can apply a similar procedure as Eq. (B4) to get $t(R)$, which in turn will provide the radius as a function of time, i.e., $R(t)$. This will eventually enable us to solve $h(r, t)$ for the depinning stage. As already noted, this solution is valid for both extensile drops (which undergo depinning without puncturing) and contractile drops.

APPENDIX D: QUASISTATIC DROP CALCULATION

We identify $\tau_{\text{surface tension}}$ as the timescale dictating the stress associates with the surface tension effect, $\tau_{\text{active stress}}$ as the timescale associated with the active stress, and τ_{evap} as the characteristic time associated with the change in drop height due to evaporation. Given that the scaling goes as $h \approx \theta_R R$, and $\nabla \approx 1/R$, from Eqs. (1a) and (1b),

$$\tau_{\text{surface tension}} \approx \frac{\mu R}{\theta_R^3 \gamma}, \quad (\text{D1})$$

$$\tau_{\text{active stress}} \approx \frac{\mu}{\theta_R^2 \xi}, \quad (\text{D2})$$

$$\tau_{\text{evap}} \approx \frac{R^2 \rho \theta_R}{D \Delta c}. \quad (\text{D3})$$

We now consider the ratio between τ_{evap} and either of the two timescales (associated with the stresses) separately. If for both the cases, τ_{evap} is found to be much larger, one can comment that the timescale for stress equilibrium is much faster than the timescale for evaporation and hence we can assume that the quasistatic drop is an excellent assumption for drop evaporation studies.

The ratio of these timescales can be expressed as

$$\frac{\tau_{\text{evap}}}{\tau_{\text{active stress}}} \approx \frac{\rho R \theta_R^3 (\xi R)}{\mu D \Delta c}, \quad (\text{D4})$$

$$\frac{\tau_{\text{evap}}}{\tau_{\text{surface tension}}} \approx \frac{\rho R \theta_R^4 \gamma}{\mu D \Delta c}. \quad (\text{D5})$$

For reference, we use the properties of water at room temperature to calculate the characteristic times, i.e., $c = 0.012 \text{ kg/m}^3$, $D = 2.4 \times 10^{-5} \text{ m}^2/\text{s}$, $\rho = 1 \text{ g/cc}$, $\mu = 0.001 \text{ Pa s}$, $\gamma = 0.072 \text{ N/m}$, and $\theta_R = 5^\circ = \frac{5\pi}{180}$. Additionally, the results in the paper are provided for $R\xi \approx 0.01\gamma$ to 0.5γ . Under these conditions, these stress ratios become

$$\frac{\tau_{\text{evap}}}{\tau_{\text{active stress}}} \sim 2 \times 10^3 - 10^5 \text{ (smallest value is for } R\xi = 0.01\gamma; \text{ greatest is for } R\xi = 0.5\gamma), \quad (\text{D6})$$

$$\frac{\tau_{\text{evap}}}{\tau_{\text{surface tension}}} \sim 1.45 \times 10^4. \quad (\text{D7})$$

-
- [1] S. Michelin, Self-propulsion of chemically active droplets, *Annu. Rev. Fluid Mech.* **55**, 77 (2023).
- [2] C. C. Maass, C. Krüger, S. Herminghaus, and C. Bahr, Swimming droplets, *Annu. Rev. Condens. Matter Phys.* **7**, 171 (2016).
- [3] J-F. Joanny and S. Ramaswamy, A drop of active matter, *J. Fluid Mech.* **705**, 46 (2012).
- [4] S. Shankar, V. Raju, and L. Mahadevan, Optimal transport and control of active drops, *Proc. Natl. Acad. Sci. USA* **119**, e2121985119 (2022).
- [5] R. Adkins, I. Kolvin, Z. You, S. Witthaus, M. C. Marchetti, and Z. Dogic, Dynamics of active liquid interfaces, *Science* **377**, 768 (2022).
- [6] S. Trinschek, F. Stegemerten, K. John, and U. Thiele, Thin-film modeling of resting and moving active droplets, *Phys. Rev. E* **101**, 062802 (2020).
- [7] K. Xie, B. Gorin, R. T. Cerbus, and L. Alvarez, Activity induced rigidity of liquid droplets, *Phys. Rev. Lett.* **129**, 138001 (2022).
- [8] D. Zwicker, J. Baumgart, S. Redemann, T. Müller-Reichert, A. A. Hyman, and F. Jülicher, Positioning of particles in active droplets, *Phys. Rev. Lett.* **121**, 158102 (2018).
- [9] A. Loisy, J. Eggers, and T. B. Liverpool, How many ways a cell can move: The modes of self-propulsion of an active drop, *Soft Matter* **16**, 3106 (2020).
- [10] C. A. Whitfield and R. J. Hawkins, Instabilities, motion and deformation of active fluid droplets, *New J. Phys.* **18**, 123016 (2016).
- [11] G. Kokot, H. A. Faizi, G. E. Pradillo, A. Snezhko, and P. M. Vlahovska, Spontaneous self-propulsion and nonequilibrium shape fluctuations of a droplet enclosing active particles, *Commun. Phys.* **5**, 91 (2022).
- [12] M. Morozov and S. Michelin, Nonlinear dynamics of a chemically-active drop: From steady to chaotic self-propulsion, *J. Chem. Phys.* **150**, 044110 (2019).
- [13] M. Morozov and S. Michelin, Self-propulsion near the onset of Marangoni instability of deformable active droplets, *J. Fluid Mech.* **860**, 711 (2019).
- [14] B. V. Hokmabad, R. Dey, M. Jalaal, D. Mohanty, M. Almukambetova, K. A. Baldwin, D. Lohse, and C. C. Maass, Emergence of bimodal motility in active droplets, *Phys. Rev. X* **11**, 011043 (2021).
- [15] J. Ignés-Mullol and F. Sagues, Active, self-motile, and driven emulsions, *Curr. Opin. Colloid Interface Sci.* **49**, 16 (2020).

- [16] S. Birrer, S. I. Cheon, and L. D. Zarzar, We the droplets: A constitutional approach to active and self-propelled emulsions, *Curr. Opin. Colloid Interface Sci.* **61**, 101623 (2022).
- [17] B. V. Hokmabad, J. Agudo-Canalejo, S. Saha, R. Golestanian, and C. C. Maass, Chemotactic self-caging in active emulsions, *Proc. Natl. Acad. Sci. USA* **119**, e2122269119 (2022).
- [18] P. Guillamat, Ž. Kos, J. Hardoüin, J. Ignés-Mullol, M. Ravnik, and F. Sagués, Active nematic emulsions, *Sci. Adv.* **4**, eaao1470 (2018).
- [19] D. Cholakova, M. Lisicki, S. K. Smoukov, S. Tcholakova, E. E. Lin, J. Chen, G. De Canio, E. Lauga, and N. Denkov, Rechargeable self-assembled droplet microswimmers driven by surface phase transitions, *Nat. Phys.* **17**, 1050 (2021).
- [20] L. Stricker, Numerical simulation of artificial microswimmers driven by Marangoni flow, *J. Comput. Phys.* **347**, 467 (2017).
- [21] B. V. Hokmabad, K. A. Baldwin, C. Krüger, C. Bahr, and C. C. Maass, Topological stabilization and dynamics of self-propelling nematic shells, *Phys. Rev. Lett.* **123**, 178003 (2019).
- [22] B. Kichatov, A. Korshunov, V. Sudakov, V. Gubernov, A. Golubkov, and A. Kiverin, Superfast active droplets as micromotors for locomotion of passive droplets and intensification of mixing, *ACS Appl. Mater. Interfaces* **13**, 38877 (2021).
- [23] M. Rajabi, H. Baza, T. Turiv, and O. D. Lavrentovich, Directional self-locomotion of active droplets enabled by nematic environment, *Nat. Phys.* **17**, 260 (2021).
- [24] T. S. Harmon and F. Jülicher, Molecular assembly lines in active droplets, *Phys. Rev. Lett.* **128**, 108102 (2022).
- [25] D. Zwicker, R. Seyboldt, C. A. Weber, A. A. Hyman, and F. Jülicher, Growth and division of active droplets provides a model for protocells, *Nat. Phys.* **13**, 408 (2017).
- [26] M. Li, M. Brinkmann, I. Pagonabarraga, R. Seemann, and J-B. Fleury, Spatiotemporal control of cargo delivery performed by programmable self-propelled Janus droplets, *Commun. Phys.* **1**, 23 (2018).
- [27] F. C. Keber, E. Loiseau, T. Sanchez, S. J. DeCamp, L. Giomi, M. J. Bowick, M. C. Marchetti, D. Zvonimir, and A. R. Bausch, Topology and dynamics of active nematic vesicles, *Science* **345**, 1135 (2014).
- [28] T. Vignaud, L. Blanchoin, and M. Théry, Directed cytoskeleton self-organization, *Trends Cell Biol.* **22**, 671 (2012).
- [29] M. N. Popescu, W. E. Uspal, C. Bechinger, and P. Fischer, Chemotaxis of active Janus nanoparticles, *Nano Lett.* **18**, 5345 (2018).
- [30] H. D. Vuijk, M. Holger, M. Lang, A. Sharma, and J. Sommer, Chemotaxis of cargo-carrying self-propelled particles, *Phys. Rev. Lett.* **126**, 208102 (2021).
- [31] C. Peng, T. Turiv, Y. Guo, Q. Wei, and O. D. Lavrentovich, Command of active matter by topological defects and patterns, *Science* **354**, 882 (2016).
- [32] A. Hölbl, L. Mesarec, J. Polanšek, A. Iglič, and S. Kralj, Stable assemblies of topological defects in nematic orientational order, *ACS Omega* **8**, 169 (2022).
- [33] J. Hu, M. Yang, G. Gompper, and R. G. Winkler, Modelling the mechanics and hydrodynamics of swimming *E. coli*, *Soft Matter* **11**, 7867 (2015).
- [34] D. Khoromskaia and G. P. Alexander, Vortex formation and dynamics of defects in active nematic shells, *New J. Phys.* **19**, 103043 (2017).
- [35] S. Čopar, J. Aplinc, Ž. Kos, S. Žumer, and R. Miha, Topology of three-dimensional active nematic turbulence confined to droplets, *Phys. Rev. X* **9**, 031051 (2019).
- [36] H. Gruler, U. Dewald, and M. Eberhardt, Nematic liquid crystals formed by living amoeboid cells, *Eur. Phys. J. B* **11**, 187 (1999).
- [37] K. Drescher, J. Dunkel, L. Cisneros, S. Ganguly, and R. E. Goldstein, Fluid dynamics and noise in bacterial cell-cell and cell-surface scattering, *Proc. Natl. Acad. Sci. USA* **108**, 10940 (2011).
- [38] Á. G. Marín, H. Gelderblom, D. Lohse, and J. H. Snoeijer, Order-to-disorder transition in ring-shaped colloidal stains, *Phys. Rev. Lett.* **107**, 085502 (2011).
- [39] Y. O. Popov, Evaporative deposition patterns: Spatial dimensions of the deposit, *Phys. Rev. E* **71**, 036313 (2005).
- [40] H. Hu and R. G. Larson, Evaporation of a sessile droplet on a substrate, *J. Phys. Chem. B* **106**, 1334 (2002).

- [41] R. D. Deegan, O. Bakajin, T. F. Dupont, G. Huber, S. R. Nagel, and T. A. Witten, Contact line deposits in an evaporating drop, *Phys. Rev. E* **62**, 756 (2000).
- [42] J. Prost, F. Jülicher, and J-F. Joanny, Active gel physics, *Nat. Phys.* **11**, 111 (2015).
- [43] A. Doostmohammadi, J. Ignes-Mullol, J. M. Yeomans, and F. Sagues, Active nematics, *Nat. Commun.* **9**, 3246 (2018).
- [44] D. Khoromskaia and G. P. Alexander, Motility of active fluid drops on surfaces, *Phys. Rev. E* **92**, 062311 (2015).
- [45] F. Jülicher, K. Kruse, J. Prost, and J-F. Joanny, Active behavior of the cytoskeleton, *Phys. Rep.* **449**, 3 (2007).
- [46] V. K. Gupta and N. L. Abbott, Using droplets of nematic liquid crystal to probe the microscopic and mesoscopic structure of organic surfaces, *Langmuir* **15**, 7213 (1999).
- [47] A. Loisy, J. Eggers, and T. B. Liverpool, Tractionless self-propulsion of active drops, *Phys. Rev. Lett.* **123**, 248006 (2019).
- [48] I. Tuval, L. Cisneros, C. Dombrowski, C. W. Wolgemuth, J. O. Kessler, and R. E. Goldstein, Bacterial swimming and oxygen transport near contact lines, *Proc. Natl. Acad. Sci. USA* **102**, 2277 (2005).
- [49] H. Hu and R. G. Larson, Analysis of the microfluid flow in an evaporating sessile droplet, *Langmuir* **21**, 3963 (2005).
- [50] H. B. Eral, D. J. C. M.'t Mannetje, and J. M. Oh, Contact angle hysteresis: A review of fundamentals and applications, *Colloid Polymer Sci.* **291**, 247 (2013).
- [51] X. Fang, K. Kruse, T. Lu, and J. Wang, Nonequilibrium physics in biology, *Rev. Mod. Phys.* **91**, 045004 (2019).
- [52] J. Freed-Brown, Evaporative deposition in receding drops, *Soft Matter* **10**, 9506 (2014).
- [53] G. He, V. Bhamidi, S. R. Wilson, R. B. H. Tan, P. J. A. Kenis, and C. F. Zukoski, Direct growth of γ -glycine from neutral aqueous solutions by slow, evaporation-driven crystallization, *Cryst. Growth Design* **6**, 1746 (2006).
- [54] A. Bar-Cohen, M. Arik, and M. Ohadi, Direct liquid cooling of high flux micro and nano electronic components, *Proc. IEEE* **94**, 1549 (2006).
- [55] J-X. Wang, W. Guo, K. Xiong, and S-N. Wang, Review of aerospace-oriented spray cooling technology, *Prog. Aerospace Sci.* **116**, 100635 (2020).
- [56] A. Ebrahimi and M. A. Alam, Evaporation-induced stimulation of bacterial osmoregulation for electrical assessment of cell viability, *Proc. Natl. Acad. Sci. USA* **113**, 7059 (2016).
- [57] N. Celika, I. Toruna, M. Ruzia, A. Esidira, and M. S. Onses, Fabrication of robust superhydrophobic surfaces by one-step spray coating: Evaporation driven self-assembly of wax and nanoparticles into hierarchical structures, *Chem. Eng. J.* **396**, 125230 (2020).
- [58] S. K. Ghosh and A. Boker, Self-assembly of nanoparticles in 2D and 3D: Recent advances and future trends, *Macromol. Chem. Phys.* **220**, 1900196 (2019).
- [59] C. Zhang, W. Li, and Y. Wang, Ultrafast self-assembly of colloidal photonic crystals during low-pressure-assisted evaporation of droplets, *J. Phys. Chem. Lett.* **13**, 3776 (2022).